

RESEARCH ARTICLE

10.1002/2016JD026251

Key Points:

- Extreme precipitation has clearly increased in recent decades across China
- The emerging signal of anthropogenic activities is detected in changes in extreme precipitation over China and is generally dominated by greenhouse gas emissions
- Large uncertainties still exist due to the effects of natural external forcings and anthropogenic aerosols

Supporting Information:

- Supporting Information S1

Correspondence to:

H. Chen,
chenhuopo@mail.iap.ac.cn

Citation:

Li, H., H. Chen, and H. Wang (2017), Effects of anthropogenic activity emerging as intensified extreme precipitation over China, *J. Geophys. Res. Atmos.*, 122, doi:10.1002/2016JD026251.

Received 16 NOV 2016

Accepted 18 JUN 2017

Accepted article online 21 JUN 2017

Effects of anthropogenic activity emerging as intensified extreme precipitation over China

Huixin Li^{1,2}, Huopo Chen^{1,3} , and Huijun Wang^{1,3}

¹Nansen-Zhu International Research Centre, Institute of Atmospheric Physics, Chinese Academy of Sciences, Beijing, China, ²College of Earth Science, University of Chinese Academy of Sciences, Beijing, China, ³Collaborative Innovation Center on Forecast and Evaluation of Meteorological Disasters, Nanjing University for Information Science and Technology, Nanjing, China

Abstract This study aims to provide an assessment of the effects of anthropogenic (ANT) forcings and other external factors on observed increases in extreme precipitation over China from 1961 to 2005. Extreme precipitation is represented by the annual maximum 1 day precipitation (RX1D) and the annual maximum 5 day consecutive precipitation (RX5D), and these variables are investigated using observations and simulations from the Coupled Model Intercomparison Project phase 5. The analyses mainly focus on the probability-based index (PI), which is derived from RX1D and RX5D by fitting generalized extreme value distributions. The results indicate that the simulations that include the ANT forcings provide the best representation of the spatial and temporal characteristics of extreme precipitation over China. We use the optimal fingerprint method to obtain the univariate and multivariate fingerprints of the responses to external forcings. The results show that only the ANT forcings are detectable at a 90% confidence level, both individually and when natural forcings are considered simultaneously. The impact of the forcing associated with greenhouse gases (GHGs) is also detectable in RX1D, but its effects cannot be separated from those of combinations of forcings that exclude the GHG forcings in the two-signal analyses. Besides, the estimated changes of PI, extreme precipitation, and events with a 20 year return period under nonstationary climate states are potentially attributable to ANT or GHG forcings, and the relationships between extreme precipitation and temperature from ANT forcings show agreement with observations.

1. Introduction

Extreme precipitation often causes greater economic losses and more destructive disasters than mean climatic conditions [Handmer *et al.*, 2012]. For example, Beijing suffered an extreme precipitation event on 21 July 2012 that caused 78 deaths and economic losses of 11.6 billion yuan [Sun *et al.*, 2012]. Previous studies have documented that the atmospheric saturation vapor pressure should scale with temperature according to the Clausius-Clapeyron (CC) equation [Trenberth *et al.*, 2003; Hardwick Jones *et al.*, 2010]. Since extreme precipitation is closely related to moisture content, the evidence indicates that extreme precipitation worldwide is increasing due to global warming [Groisman *et al.*, 2005; Alexander *et al.*, 2006; Westra *et al.*, 2013]. Furthermore, the occurrence of extreme precipitation events is projected to increase significantly in the future due to additional warming [Sun *et al.*, 2010; Chen *et al.*, 2012a; Chen and Sun, 2015]. Given the importance of changes in extreme precipitation, the question arises as to whether anthropogenic activity or other factors have contributed to the intensification of extreme precipitation.

Numerous studies have suggested that human influence intensifies extreme precipitation events on a global scale [Min *et al.*, 2009, 2011; Zhang *et al.*, 2013]. Specifically, the Fifth Assessment Report of the Intergovernmental Panel on Climate Change indicated that anthropogenic forcing has intensified extreme precipitation globally with medium confidence [Bindoff *et al.*, 2013]. However, the evidence has only demonstrated an anthropogenic contribution on a global scale. Few studies have considered subcontinental scales due to the reduction in detectability caused by lower signal-to-noise ratios [Zhang *et al.*, 2013]. Despite the substantial uncertainties and limitations associated with such studies, it is also necessary to assess anthropogenic effects on extreme precipitation at national scales, as this can improve our knowledge of model performance at smaller scales and our ability to project future changes in extreme precipitation. Further, it helps us to provide the information needed to diminish the potential risks.

There are different approaches to detecting and attributing climatic events and changes [Stott *et al.*, 2010, 2016]. For example, Fischer and Knutti [2015] employed the “fraction of attributable risk” (FAR) and the

“probability ratio” (PR) to evaluate the effects of human activity on heavy precipitation events worldwide. The PR is defined as P_1/P_0 , and the FAR is defined as $1 - (P_1/P_0)$, where P_0 (or P_1) is the probability of exceeding a certain quantile during the preindustrial control period (or the given period). Schaller *et al.* [2016] used the “end-to-end” method to assess the degree of human influence on winter floods in southern England during 2014. In this study, physical principles are embodied in climate models that can directly estimate the climatic response to external forcings [Sun *et al.*, 2016]. In our study, we use the rigorous optimal fingerprint method to detect and assess attributable changes in extreme precipitation response to external forcings [Allen and Tett, 1999; Allen and Stott, 2003]. This method provides specific analyses of the associations between external forcings and observed climate changes. This optimal detection method has been widely used to detect and attribute temperature changes both globally [Ribes and Terray, 2013] and regionally [Zwiers *et al.*, 2011; Sun *et al.*, 2014; Xu *et al.*, 2015; Sun *et al.*, 2016]. Additionally, Min *et al.* [2011] primarily used the fingerprint method to detect and attribute probability-based extreme precipitation on a global scale. Based on this method, Mondal and Mujumdar [2015] successfully identified the effects of the anthropogenic forcings on extreme precipitation over India.

Previous studies have documented that extreme precipitation events during the past decades have intensified over most regions of China [Chen *et al.*, 2012b; Wang *et al.*, 2012; Sun and Ao, 2013; Liu *et al.*, 2015; Fan and Chen, 2016]. The influence of anthropogenic effects has been detected in this change, but with large uncertainties [Chen and Sun, 2017]. Thus, more work is needed to investigate this aspect. Therefore, the rigorous optimal fingerprint approach [Allen and Tett, 1999; Allen and Stott, 2003] is applied in this study to detect and attribute the intensification of extreme precipitation events across China.

2. Data

The observational data sets employed in this study are the gridded daily precipitation data set and the gridded monthly temperature data set (hereafter referred as CN05) developed by Wu and Gao [2013]. CN05 was produced via interpolation using the “anomaly approach” and employed 2416 stations in China, and it has a high spatial resolution of $0.25^\circ \times 0.25^\circ$. For detailed information about the process of constructing and interpolating these data sets, please refer to Xu *et al.* [2009]. In this study, only the data sets from 1961 to 2005 are used to conform to the different time periods covered by model simulations.

For the purpose of detection and attribution analyses, 15 models from the Coupled Model Intercomparison Project phase 5 (CMIP5), including different runs, were obtained from the website of the Earth System Grid gateway hosted by the Program for Climate Model Diagnosis and Intercomparison. Multimodel simulations for different experiments that represent historical natural forcing (NAT; e.g., volcanic eruptions and solar activity), historical greenhouse gases (GHG), and historical natural plus anthropogenic forcings (ALL) are employed to investigate the effects of these factors on the intensification of extreme precipitation over China. Table 1 lists relevant information about these models, which provide gridded data sets of historical daily precipitation from the NAT, ALL, and GHG simulations and unforced control (CTL) simulations; the CTL simulations include 188 segments of a nonoverlapping 45 year sample. Furthermore, the historical anthropogenic forcings (ANTs; ALL minus NAT) and other anthropogenic forcings (OA; ANT minus GHG, including aerosols and land use, as well as other factors) are also considered in our study. We assume that the differences between the ALL and NAT simulations represent the linearly additive response to the external forcings [Zhang *et al.*, 2013]. Thus, ANT is estimated as ALL minus NAT. Since ANT considers OA in addition to GHG, OA is indirectly estimated as ANT minus GHG. Moreover, the corresponding gridded monthly temperature data sets used in this study are available.

Previous studies have used various definitions of extreme precipitation, such as given thresholds and percentile thresholds. Here the annual maximum 1 day precipitation (RX1D) and the annual maximum 5 day consecutive precipitation (RX5D) will be analyzed. RX1D represents the magnitude of extreme precipitation, whereas RX5D is the cumulative value, which is relevant in assessing the risks of flooding disasters. Both metrics are good indicators of extreme precipitation events [Westra *et al.*, 2013]. In general, the estimation of spatially averaged extreme precipitation is uncertain due to high spatial variability and sparse observational network but we can circumnavigate this issue by transforming annual extreme precipitation values

Table 1. List of the 15 Climate Models That Contributed Historical Simulations to CMIP5^a

	NAT (No. of Runs)	ALL (No. of Runs)	GHG (No. of Runs)	CTL (No. of 45 Year Chunks)
BCC-CSM1.1	1	3	1	11
BNU-ESM	1	1	1	12
CanESM2	5	5	5	24
CCSM4	4	3	3	3
CNRM-CM5	6	10	6	18
CSIRO-Mk3.6.0	5	10	5	11
GFDL-CM3	3	5	3	17
GFDL-ESM2M	1	1	1	11
HadGEM2-ES	4	4	4	12
IPSL-CM5A-LR	3	6	6	22
IPSL-CM5A-MR	3	3	3	6
MIROC-ESM	3	3	3	14
MIROC-ESM-CHEM	1	1	1	5
MRI-CGCM3	1	5	1	11
NorESM1-M	1	3	1	11
Total	42	63	44	188

^aThese simulations include NAT (natural forcing), ALL (natural plus anthropogenic forcing), and GHG (greenhouse gas forcing) runs covering the period from 1961 to 2005 and CTL (preindustrial control) simulations. The numbers in the first three volumes represent the ensemble members with external forcings, and the rightmost volume indicates the number of 45 year nonoverlapping sections of the CTL runs.

into probability-based indices (PIs) [Min et al., 2011]. As is widely known, the changes in extreme precipitation over China vary among the different regions [Wang et al., 2013; Ren et al., 2015; Li et al., 2016a, 2016b]. Thus, the PI, which is derived from RX1D and RX5D, will be used to reduce the uncertainty of the spatial averages and improve the intercomparability of the data sets.

Here it should be noted that, because of the absence of measurement sites over most of the Tibetan Plateau that is located in southwestern China, the data sets covering the Tibetan Plateau are masked out in both the observations and the models.

3. Methods

3.1. Probability-Based Index Calculation

We have preprocessed the observational data sets and the individual model simulations by interpolating daily precipitation values onto 1.5° × 1.5° grid cells using the first-order conservative remapping method. The observed and simulated extreme precipitation metrics (RX1D and RX5D) under different forcings are then calculated from the 1.5° × 1.5° gridded daily precipitation data sets.

Overall, the characteristics of changes in extreme precipitation over China display a regional dependence [Chen et al., 2012b]. To improve the comparability and representativeness of our research, the PI is derived from the extreme precipitation metrics (RX1D and RX5D) by fitting the generalized extreme value (GEV) distribution to the data from each grid point within China [Min et al., 2011; Zhang et al., 2013; Zhang and Zwiers, 2013]. The PI is estimated as the result of the cumulative distribution function (CDF) derived from the GEV distribution of RX1D and RX5D, as shown in equation (1) [Wilks, 2011]. The CDF of the GEV is a function of three variables, the location (ζ), scale (β), and shape (κ), which can be estimated using the maximum likelihood method [Martins and Stedinger, 2000]. Clearly, the PI ranges from zero and unity, and stronger extreme precipitation yields a larger PI. Accordingly, we calculate in advance the observed and simulated PI values for RX1D and RX5D at each grid point.

$$PI(x) = \exp \left\{ 1 + \left[\frac{\kappa(x - \zeta)}{\beta} \right]^{-\frac{1}{\kappa}} \right\}, \kappa \neq 0, 1 + \frac{\kappa(x - \zeta)}{\beta} > 0$$

$$PI(x) = \exp \left\{ -\exp \left[-\frac{(x - \zeta)}{\beta} \right] \right\}, \kappa = 0$$
(1)

3.2. Detection and Attribution Method

The optimal fingerprint method provides rigorous attribution and detection analysis of extreme precipitation over China. It is described by the following regression model [Ribes *et al.*, 2013]:

$$y = \sum_{i=1}^n \beta_i x_i + \varepsilon \quad (2)$$

$$\tilde{x}_i = x_i + \varepsilon_{x_i} \quad (3)$$

In equation (2), y denotes the observations, x_i is the climatic response to the i th external forcing employed (including NAT, GHG, ANT, OA, and ALL), β_i is the scaling factor that adjusts the fingerprint value to produce the best match to the observations, n denotes the number of external forcings considered, and ε represents the internal climate variability (a residual term that is estimated from the CTL simulations). Here we assume that x_i is unknown, and \tilde{x}_i is calculated from the ensemble mean that has a random term related to internal variability (ε_{x_i} ; see equation (3)). To examine the reliability of the residual term, the corresponding residual consistency test [Allen and Stott, 2003] is conducted in our study. Notably, the CTL simulations are divided into 188 segments representing nonoverlapping 45 year samples. Half of these segments are used to estimate the regression coefficients, and the other half are used to conduct a residual consistency test to avoid spurious detections.

In this study, the attributable PI changes are investigated by multiplying the PI trends by the corresponding 5–95% marginal scaling factors, and the results are further multiplied by the 45 year period. The observed PI changes and its 90% confidence intervals (5%–95%, based on the least squares method) are calculated as the PI trends multiply by the corresponding 45 year temporal coverage. In addition, we would like to determine how RX1D and RX5D might change under nonstationary climatic conditions. Thus, we further convert these attributable and observed PI changes to possible percent changes in extreme precipitation.

Evidence indicates that extreme precipitation over China intensified (see section 4.1) from 1961 to 2005. Thus, the GEV distribution based on stationary climatic conditions should extend to nonstationary climatic conditions [Katz, 2013]. Due to the enhanced internal variability and intermodel uncertainty seen at regional scales, it is difficult to determine how PI changes within each grid cell within China respond to different forcings. Thus, we assume that only the location parameter (ξ) in equation (1) changes with time at each grid point over China, and the same attributable PI changes (δPI) are applied to all of the grid cells [Zhang *et al.*, 2013]. Here we first calculated the median value of extreme precipitation (X_{50} , where PI equals 0.5) at individual grid cell over China. Then, the two new location parameters ξ_0 (which corresponds to the year 1961) and ξ_1 (which corresponds to the year 2005) are computed as that X_{50} has probabilities of $0.5 - \frac{\delta PI}{2}$ and $0.5 + \frac{\delta PI}{2}$, and the percent change in the median value of extreme precipitation is computed as $\frac{100 \times (\xi_1 - \xi_0)}{\xi_0}$ at each grid point. Finally, we can compute the area-weighted average of the percent change in the median value of extreme precipitation over China, and the confidence ranges spanning the 90% confidence level are obtained in the same way.

In general, the return value and return period provide valuable information for assessing the risks of extreme events [Aghakouchak *et al.*, 2014], and an event with a return period of T years corresponds to a $1/T$ probability of occurrence in any particular year [Cooley *et al.*, 2007]. The return period is calculated based on the GEV distribution to discuss changes in extreme events under nonstationary climatic conditions. As shown in equation (4), the return period $R(x)$ can be explained by the CDF value $F(x)$, where $\omega = 1 \text{ year}^{-1}$ is the average sampling frequency [Wilks, 2011]. Given a particular return period, it is easy to compute the return values and vice versa. Based on the above assumptions, we use equation (4) to compute the 20 year return values at each grid point with the location parameter associated with the beginning of the study period ξ_0 (which corresponds to the year 1961) in equation (1). Similarly, the new return periods of these return values are computed using the GEV distribution with the location parameter associated with the end of the study period ξ_1 (which corresponds to the year 2005). Estimates of the attributable and observational area-weighted average of return period are then obtained, and confidence ranges that span the 90% confidence level are calculated in the same way.

$$R(x) = \frac{1}{\omega[1 - F(x)]} = \frac{1}{\omega[1 - PI(x)]} \quad (4)$$

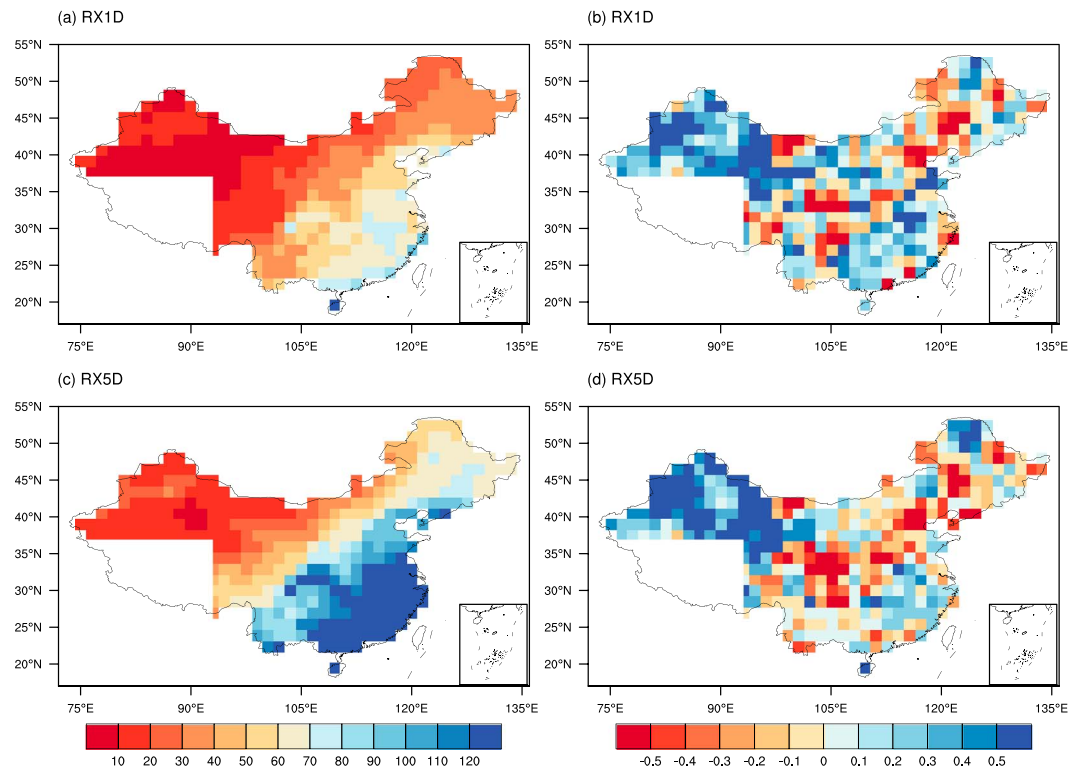


Figure 1. Climatological spatial distribution of observed extreme precipitation from 1961 to 2005 for (a) RX1D and (c) RX5D and (b) and (d) the corresponding PI trends. Units for RX1D and RX5D: mm d^{-1} .

4. Results

4.1. Characterizing Extreme Precipitation Over China

Figure 1 shows the spatial pattern of annual extreme precipitation over China from 1961 to 2005, as calculated from CN05, and the corresponding PI trends. The amount of extreme precipitation decreases significantly from the southeast to the northwest in China based on RX1D (Figure 1a) and even more significantly when RX5D is considered (Figure 1c). In terms of trends in the PI, positive values indicate stronger extreme precipitation events, while negative values indicate weaker events. There is a clear overall increasing trend in the PI in most regions of China; 64% of the regions have positive RX1D values (Figure 1b), and 57% of the regions have positive RX5D values (Figure 1d). However, the spatial distribution of the PI trend shows a strong regional dependence. The regions that display decreasing trends are mainly located in the northern, northeastern, and eastern-southwestern parts of China, as well as the coastlines of southeast China, in accordance with previous studies [Zhai *et al.*, 2005; Chen *et al.*, 2012b; Wang *et al.*, 2012]. Additionally, RX5D exhibits a broadly decreasing trend in the regions of central China.

Figure 2 presents the spatial distribution of trends in the PI for RX1D from the multimodel ensemble mean (MME), and the results for RX5D are shown in Figure 3. The results from the NAT simulations show weak trends almost everywhere, with low intermodel agreement across China (Figures 2a and 3a). In detail, the decreasing trends seen in some parts of northern China are consistent with observations, although they have smaller amplitudes. However, the decreasing trends seen in northwestern and southeastern China are opposite to those seen in the observations, resulting in a weak pattern correlation coefficient of 0.03 between CN05 and the NAT simulations for RX1D and a pattern correlation coefficient of -0.01 for RX5D over China. The results from the GHG simulations show an overall increasing trend (Figures 2b and 3b), and high intermodel agreement is seen in most regions of China. Increasing trends can be clearly seen in northwestern and southeastern China in the observations. However, the GHG simulations fail to reproduce the decreasing trends observed in northeastern China and some parts of southwestern China. The pattern correlation coefficients between the results of the GHG simulations and CN05 are 0.28 for RX1D and 0.19 for RX5D, both of which are significant at the 99% confidence level, based on Student's *t* test. Compared to the GHG

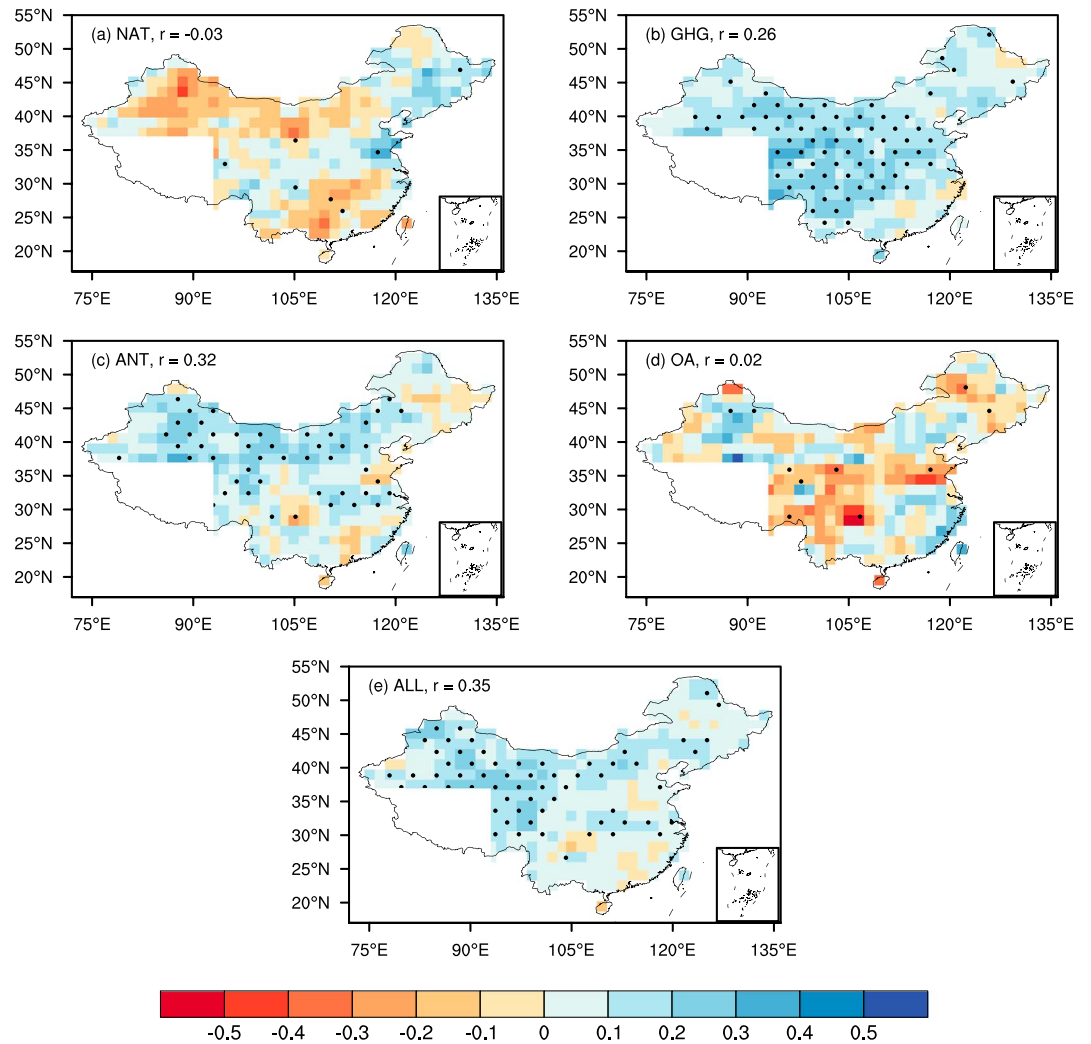


Figure 2. Spatial distribution of the PI trend based on RX1D from 1961 to 2005 established using an MME based on (a) natural (NAT) forcings, (b) greenhouse gas (GHG) forcings, (c) anthropogenic (ANT) forcings, (d) other anthropogenic (OA) forcings, and (e) anthropogenic plus natural (ALL) forcings. Values represent spatial correlations between the MME, which consists of 15 models, and CN05. The black dotted areas indicate that more than 60% of the 15 models share the same sign as the trend seen in the MME.

simulations, the ANT results display substantially improved performance and provide more explicit spatial information than the GHG simulations. As shown in Figures 2c and 3c, regions with high intermodel agreement are located in the northwestern and western-northern parts of China and the Yangtze River region, and these results resemble the observations. Generally, the ANT results show positive trends in most regions, but they show negative trends in the northeastern, eastern-southwestern, and southeastern coastal regions of China. In contrast, the OA results exhibit an overall decreasing trend in most regions of China, especially over northeastern and eastern-southwestern China. However, large differences can be observed among the models across China. The pattern correlation coefficient between the OA results and CN05 is insignificant, but the influence of the OA forcings, which is unfavorable for the increasing trend in the PI over northeastern and southwestern China, cannot be neglected (Figures 2d and 3d). Consequently, the OA forcings play an important role in offsetting the increasing trend seen in some regions due to GHG, and the ANT results display better performance than the GHG simulations. The significant pattern correlation coefficients between the ANT results and CN05 are 0.32 for RX1D and 0.33 for RX5D, respectively. The results from the ALL simulations (Figures 2e and 3e) present a pattern similar to that of the ANT results, with higher pattern correlation coefficients of 0.35 for both RX1D and RX5D. Regions with obvious increasing trends display high intermodel

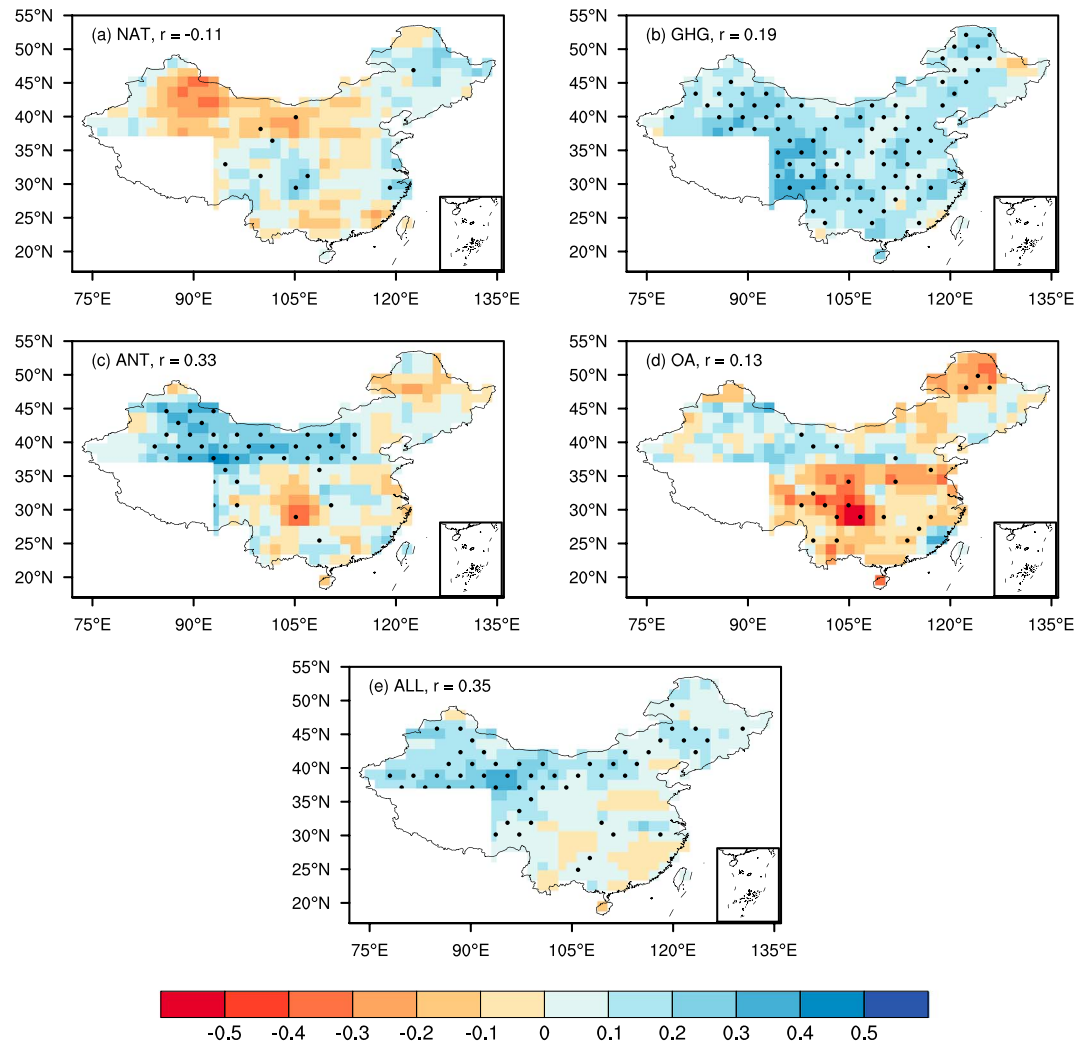


Figure 3. Same as in Figure 2 but for RX5D.

agreement, which also presents a considerable similarity with the observations. However, offset by the decreasing trend in northwest and southeastern China caused by the NAT forcings, the amplitudes over these regions seen in the ALL simulations are weaker than those seen in the ANT results.

To characterize the temporal variation in extreme precipitation, Figure 4 displays 5 year mean, spatially averaged PI anomalies over China. The temporal evolution of the PI reflects a general increase from 1961 to 2005, but it includes a profound decrease that began in the early 2000s over China (Figures 4a and 4b). The upward trends in the MME seen in the GHG, ANT, and ALL simulations are substantially similar to those of the observations, in spite of their weaker amplitudes. However, the NAT simulations show no obvious trend from 1961 to 2005, whereas the OA results show a decreasing trend. These results are quite reliable because the spatially averaged temporal variations for the individual external forcings have the same sign as the corresponding spatial patterns, especially in those regions with high intermodel agreement (see Figures 2 and 3). Thus, the spatially averaged PI anomalies over China represent the leading spatial information and temporal variations in the PI trends, making the analyses of detection and attribution quite reliable. As with the spatial pattern, we also focus on the intermodel agreement for each forcing, and the results of the various simulations indicate that 60% (73%) of OA, 53% (60%) of NAT, 93% (93%) of GHG, 93% (73%) of ANT, and 100% (93%) of ALL have the same signs as the trends seen in the PI for RX1D (RX5D). The results from these models are then chosen for further analysis in Figures 4c and 4d. Clearly, the major features are similar to those of Figures 4a and 4b, but some of the magnitudes are higher.

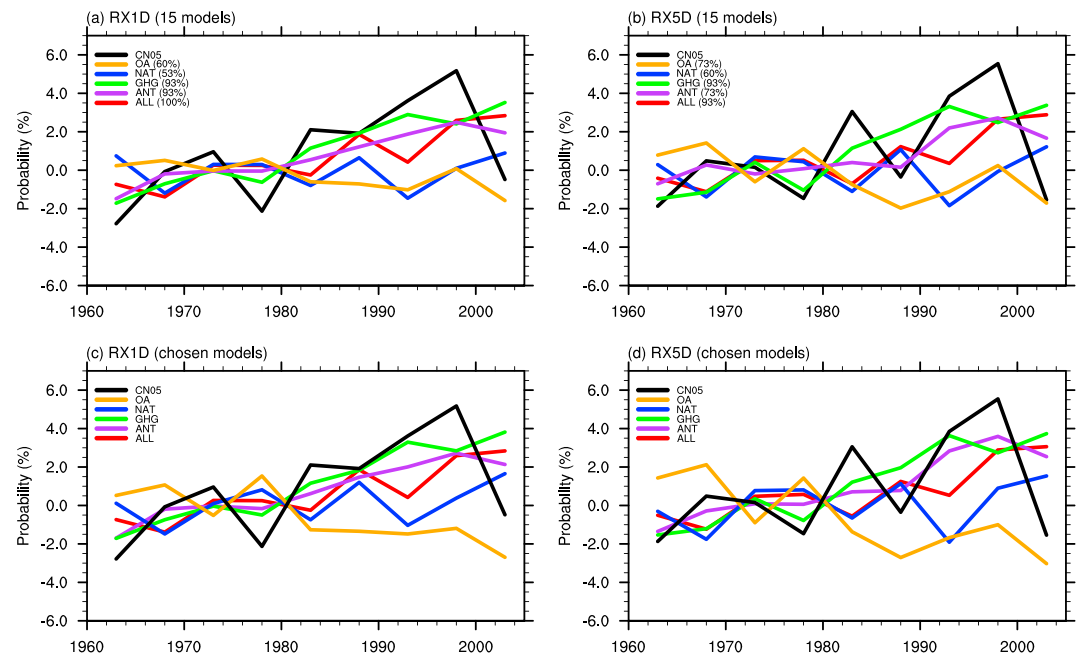


Figure 4. Five-year mean temporal series of the spatially averaged PI anomalies (relative to the climatology of 1961–1990) over China from 1961 to 2005 for (a) RX1D and (b) RX5D, based on the MME containing 15 models. Values in the parentheses in Figures 4a and 4b represent the degree of intermodel agreement based on the individual model results for each forcing, (c and d) while RX1D and RX5D based on the MME containing the selected models are displayed, respectively.

In addition to the spatial and temporal characteristics of the PI trends, we are also interested in the climatological conditions of the PI anomalies during different decades. Because the spatially averaged PI increased by approximately 5% from 1961 to 2005, we divide this increment into two equal parts (0.025). Figure 5 shows the spatial distribution of the PI anomalies (relative to the climatology of 1961–1990) that are lower than -0.025 from 1961 to 1980 and higher than 0.025 from 1986 to 2005. During the first period, the regions with lower PI values are mainly located in northwestern China, the Yangtze River Valley, and parts of northeastern China (Figures 5a and 5c). These regions correspond to the regions with higher PI values in the latter period (Figures 5b and 5d). In turn, these regions indicate the maximum increase in the PI over China. Thus, the increments over these regions subsequently account for the increasing trend in the PI averaged over China. Likewise, the ANT results also indicate an increasing trend in the PI over northwest China, but they underestimate the PI anomalies and do not reproduce the increasing trend over the Yangtze River Valley and northeastern China (Figure 6). All of the pattern correlation coefficients between the ANT results and CN05 are significant at the 99% confidence level, based on Student's *t* test. However, we note that the intermodel agreement is quite low for both decades, which mainly results from the smaller increment of the PI obtained from the ANT results. In fact, the increment of the PI values estimated using the ANT results is about half that of CN05 (see Figure 4), and regions with high intermodel agreement resemble the observations if we focus on the 2.5% increment (see Figure S1 in the supporting information). The results from the ALL simulations show a pattern similar to that of the ANT results; however, the amplitude is weaker (figures not shown). In addition, the GHG simulations show less consistency with the observations because, in this case, the regions that show major increases in the PI are located between the latitudes of 28 and 38°N over China, rather than in northwestern China (figures not shown).

In general, some of the forcings (e.g., ANT, GHG, and ALL) can account for the observed changes both spatially and temporally, whereas the others cannot. The detection analysis in the following section is conducted based on the area-averaged temporal series that can be calculated from the selected models.

4.2. One-Signal and Two-Signal Detection of the PI

To detect the effects of a given external forcing on changes in extreme precipitation over China, optimal fingerprint methods are employed. According to equations (2) and (3), the 5 year mean-observed PI series are

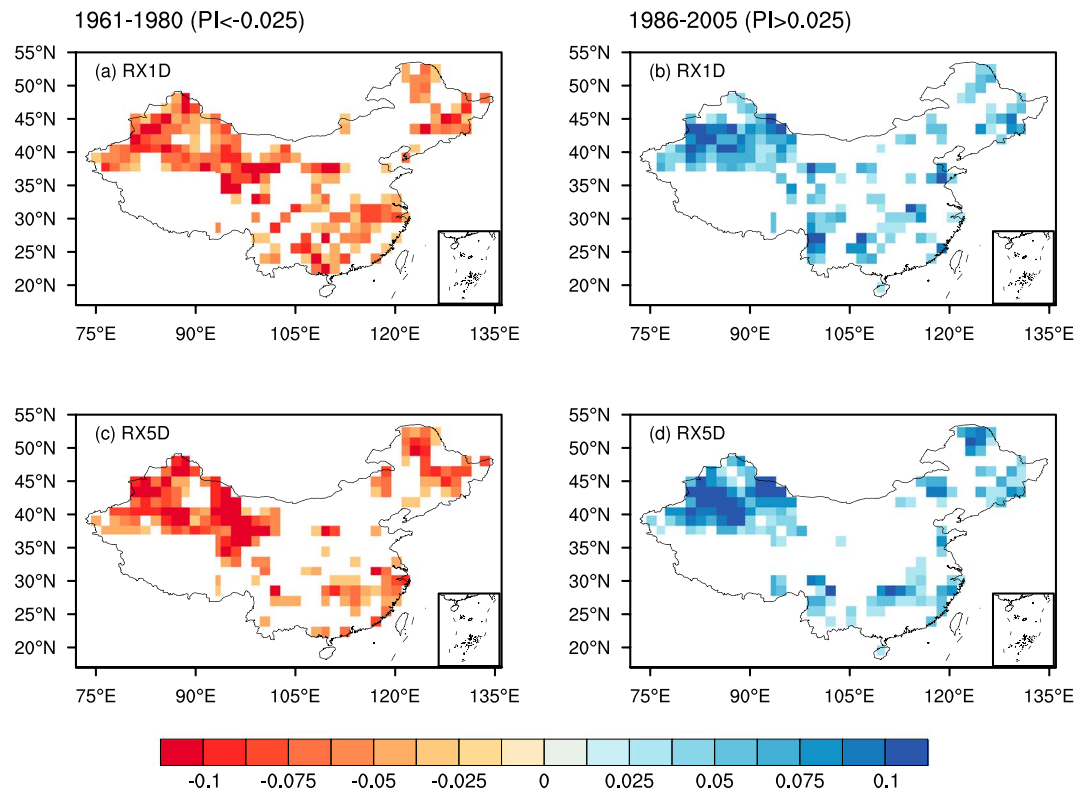


Figure 5. The observed spatial distribution of the averaged PI anomalies (relative to the climatology of 1961–1990) during the earlier period (1961–1980) with values less than -0.025 for (a) RX1D and (c) RX5D and during the later period (1986–2005) with values greater than 0.025 for (b) RX1D and (d) RX5D.

regressed onto the MME consisting of the 15 models and the MME containing the selected models, both of which employ the different external forcings (ALL, ANT, GHG, NAT, and OA). The amplitude of the scaling factor explains the fingerprint of the external forcing present in the observations. Its uncertainty range (5%–95%) should be greater than zero to ensure that the PI is detectable in the model simulations. Moreover, if the uncertainty range also includes unity, the model simulation is considered to be in accordance with observations.

Figure 7 shows the scaling factors of the 5 year mean PI series for the MME that includes the selected models. The results obtained using the MME that includes all 15 models are similar, except for their larger uncertainty ranges (see Figure S2). The standard residual consistency test indicates that the null hypothesis of the observational PI being equal to that of the MME cannot be rejected at the 90% confidence level (all of the p values are larger than 0.1), suggesting that these regression models fit the data well. For single-signal cases, the GHG signal is detectable in RX1D (Figure 7a) but not in RX5D (Figure 7c). The best estimate of the GHG fingerprint in RX1D is near unity, indicating good consistency with the observations. In contrast, the effects of the OA forcings are not detected in RX1D and RX5D, and the 90% confidence intervals of the scaling factors are negative. The negative scaling factors suggest the opposing effects of anthropogenic aerosols, which partially offset the increasing role of the GHG forcings. Because the OA-only regression model lacks the primary component of a predictor, it is an invalid regression model. Despite the failure to detect the OA forcings in both RX1D and RX5D, as well as the failure to detect the GHG forcings in RX5D, their combined forcings (ANT) are detectable. The 90% confidence intervals of the scaling factor for the ANT results exclude zero and include unity in both RX1D (Figure 7a) and RX5D (Figure 7c). The best estimate is larger than unity, suggesting an underestimation of the observed PI changes. The resulting spatial patterns and temporal series also support these analyses. Accordingly, the effects of the OA forcings optimize the fingerprint of the ANT forcings detected in the observations compared to the GHG simulations, whereas the GHG simulations primarily account for the detected responses in the ANT results. However, the 90% uncertainty ranges of the

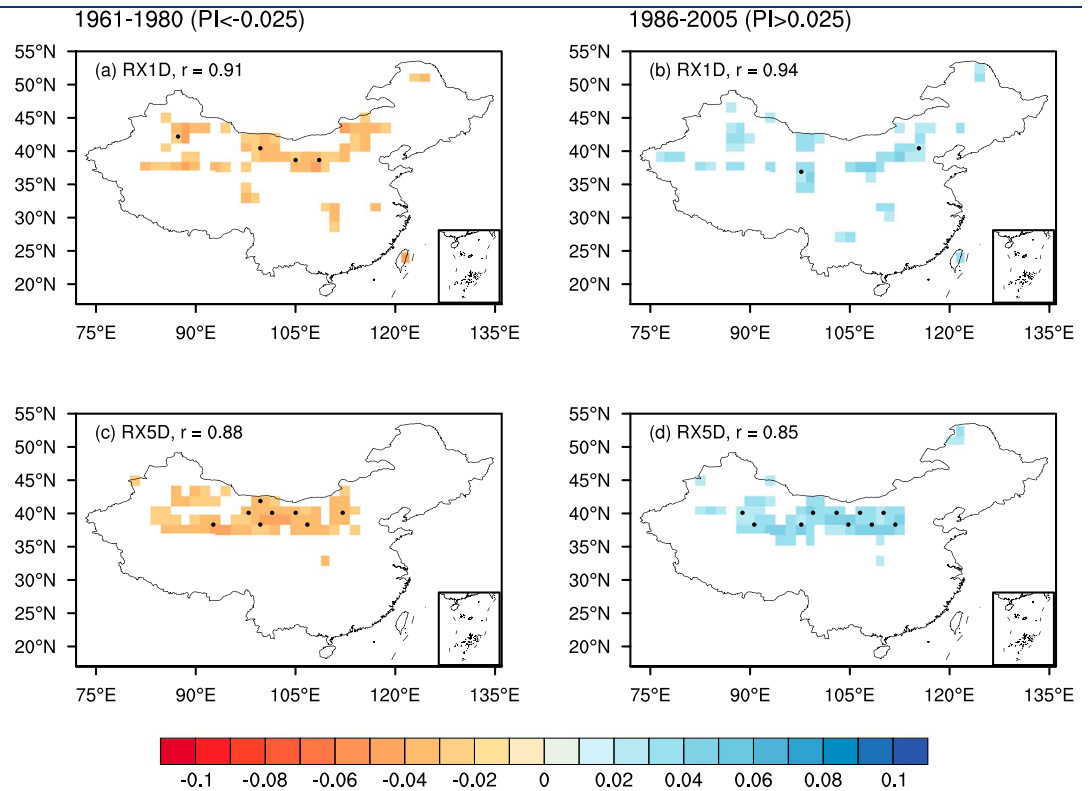


Figure 6. Same as in Figure 5 but based on the ANT results derived from the MME. The values represent the pattern correlation between the ANT results and CN05, and the black dotted areas indicate that more than 60% of the 15 models have the same sign as the trend in the MME.

fingerprints describing the responses to the ALL and NAT forcings include zero in both RX1D (Figure 7a) and RX5D (Figure 7c). Thus, these experiments fail to detect the trend in the PI over China. Here the exclusion of the primary predictor (e.g., the ANT forcings) renders the NAT-only regression model invalid [Zhang *et al.*, 2013]. Consequently, the NAT forcings are likely responsible for the failure to detect using the ALL simulations. Similarly, we further focus on the detectability response to different forcings when the internal variability is doubled (the dashed lines in Figures 7a and 7c), and the results indicate that all of the simulations fail to detect the PI changes over China, indicating that a decline in robustness occurs as the internal variability becomes stronger.

To separate the individual contributions from the combined effects, two-signal analyses are also carried out in our study (Figures 7b and 7d). We focus on two combinations that include the ANT and NAT forcings and the GHG and no-GHG forcings (including the NAT and OA forcings). The best estimate of ANT in the two-signal case is larger than unity, also suggesting a possible underestimation of the response to the ANT forcings by the models. However, the scaling factor associated with the NAT forcings includes zero, indicating that the NAT forcings cannot be detected in the two-signal analyses. Consequently, the ANT and NAT forcings cannot be jointly detected, but the effects of the ANT forcings can be separated from those of the NAT forcings in the two-signal analyses. For the combination of the GHG and no-GHG forcings, the ranges of both of the scaling factors include zero; thus, these forcings are not detected. In addition, the GHG and no-GHG forcings cannot be jointly detected. Hence, only the ANT forcings provide a satisfactory explanation of the observed changes in the PI from 1961 to 2005. Although the GHG forcings can explain the observed changes in the PI in the single-signal analyses using RX1D, its effect cannot be separated from those of the no-GHG forcings. Additionally, the fingerprints of each forcing are still not detectable with doubled internal variability, as reflected by the dashed lines in Figures 7b and 7d.

4.3. Attributable Changes Under Nonstationary Climate Conditions

The optimal fingerprint method provides us with knowledge of the detection of the PI trends in response to external forcings. In the following, we further estimate changes in extreme precipitation using simulations

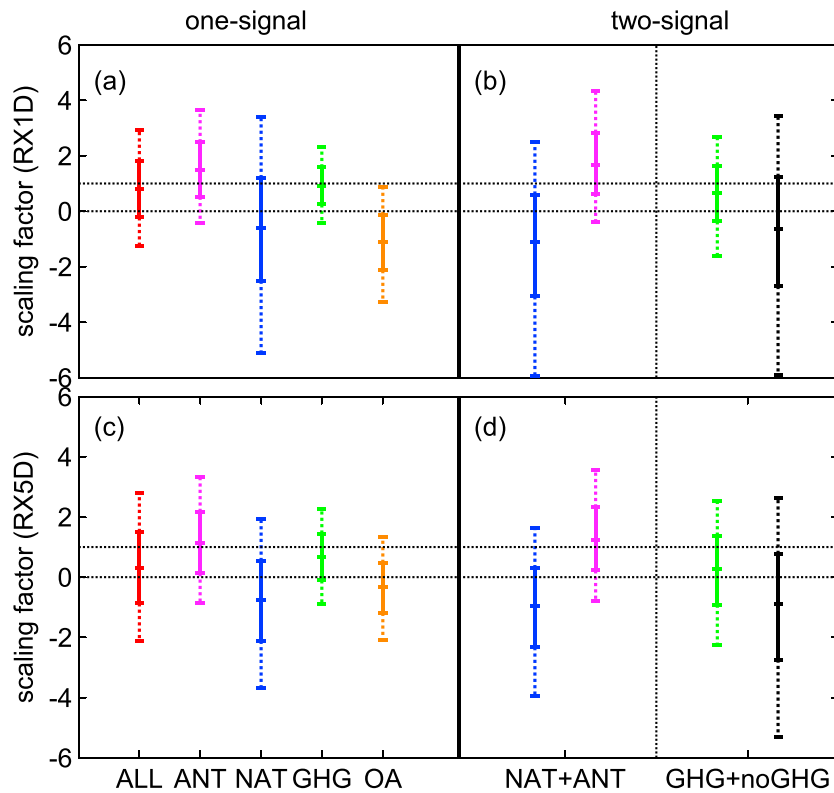


Figure 7. Scaling factors resulting from the optimal fingerprint analyses of the PI values for (a and b) RX1D and (c and d) RX5D using single-signal (Figures 7a and 7c) and two-signal (Figures 7b and 7d) analyses, respectively. The solid lines indicate the 5–95% uncertainty range of the scaling factor, and the dashed error bars are the results for doubled internal variability. The two dashed horizontal black lines represent the unity and zero. The results are based on the MME containing the selected models.

that include the ALL, ANT, NAT, GHG, and OA forcings to reveal their corresponding influences. To address this issue, we first estimate the attributable PI changes from 1961 to 2005 based on the selected models (Figure 8). The results based on the 15 models are similar, except that the ranges associated with NAT vary among the models (see Figure S3). PI is observed to increase by 5.14% (0.29% to 10%) for RX1D (Figure 8a) and 3.75% (–1.89% to 9.39%) for RX5D (Figure 8b), indicating that the intensification of RX1D is larger. More information referring to the estimation of δPI can be found in section 3.2. δPI is estimated to be 6.61% (2.32% to 11.26%) for the ANT forcings and 5.70% (1.54% to 9.97%) for the GHG forcings, both of

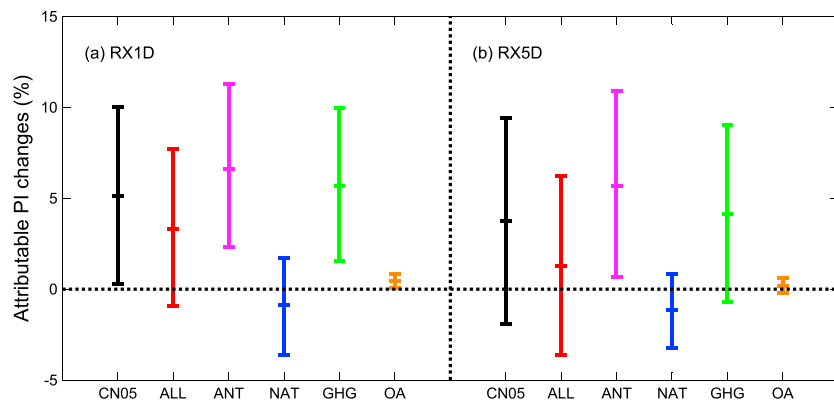


Figure 8. Best estimates of observed PI trends and the attributable changes in the PI due to the ALL, ANT, NAT, GHG, and OA forcings from 1961 to 2005 for (a) RX1D and (b) RX5D. The error bars indicate the 90% confidence intervals. Unit: %. The results are based on the MME containing the selected models.

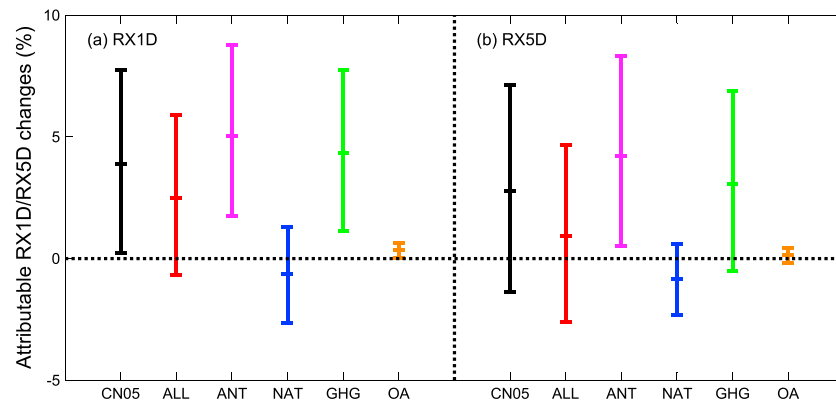


Figure 9. Same as in Figure 8 but for the observed and attributed changes in extreme precipitation under nonstationary climate conditions from 1961 to 2005 for (a) RX1D and (b) RX5D. Units: %.

which are consistent with observations. Here δPI of the OA forcings is only 0.44% (0.05% to 0.85%), which is much smaller when compared to the GHG forcings. Despite the negligible PI changes attributable to the OA forcings, the joint role of the OA and GHG forcings leads to a larger increase in the attributable PI changes obtained using the ANT results than that obtained using the GHG simulations. Furthermore, the estimate of the PI changes attributable to the NAT forcings exhibits a decreasing trend, weakening the increasing trend seen in the ANT results and resulting in a lower median value and a reduced consistency with the observations in the ALL simulations. For the attributable PI changes using RX5D (Figure 8b), δPI is estimated to be 5.65% (0.68% to 10.89%) for the ANT forcings and 4.12% (−0.69% to 9.05%) for the GHG forcings, and these results also display good consistency with the observations. The changes in OA are negligible, but the combined effect of the GHG and OA forcings also produces a larger increase in the ANT results than in the GHG simulations. Similar to RX1D, the PI changes attributable to the NAT forcings are almost negative for RX5D, partially offsetting the positive changes caused by the ANT forcings and thus leading to underestimates of the PI changes attributable to the ALL forcings. Accordingly, the ANT forcings (including the GHG forcings) played an emerging role in producing the observed PI changes from 1961 to 2005. Despite the negligible value attributable to the OA forcings, the joint role of the GHG and OA forcings is larger than that of the GHG forcings. Moreover, the negative δPI due to the NAT forcings weakens the effects of the ANT forcings, leading to a reduction in the PI changes attributable to the ALL forcings than that associated with the ANT forcings.

In general, changes in extreme precipitation are more intuitive when compared to changes in the PI. We therefore convert these attributable PI changes to the attributable percent changes in extreme precipitation response to different forcings. Given the limitations imposed by the restrictions of model data sets at small scales indicated in section 3.2, it is difficult to detect and attribute the PI changes within each grid cell over China. To simplify the problem, we assume that, under nonstationary climate conditions, all of the grid cells over China share the same δPI value calculated in the above analyses [Zhang *et al.*, 2013]. In addition, all of the locations have their individual GEV distributions. Based on these assumptions, the possible percent changes in RX1D and RX5D are analyzed and compared. Figure 9 shows the estimates of the observed and attributable percent changes in extreme precipitation for the selected models. The results for the 15 models are similar (see Figure S4). Extreme precipitation is estimated to have increased by 3.90% (0.22% to 7.76%) for RX1D (Figure 9a) and 2.77% (−1.37% to 7.13%) for RX5D (Figure 9b) over the study period. The attributable percent changes in extreme precipitation for RX1D (Figure 9a) are estimated to correspond to increases of 5.05% (1.73% to 8.79%) for the ANT forcings and 4.33% (1.15% to 7.73%) for the GHG forcings, both of which are in accordance with observations. The responses attributable to the ANT forcings are stronger than those attributable to the GHG forcings, which also resulted from the combined effect of the GHG and OA forcings. In addition, due to the offset produced by the NAT experiment, the attributable value for the ALL forcings is only 2.50% (−0.68% to 5.90%), which is smaller than that of the observations. Additionally, the attributable changes in extreme precipitation for RX5D (Figure 9b) are estimated to represent increases by 4.21% (0.50% to 8.33%) for the

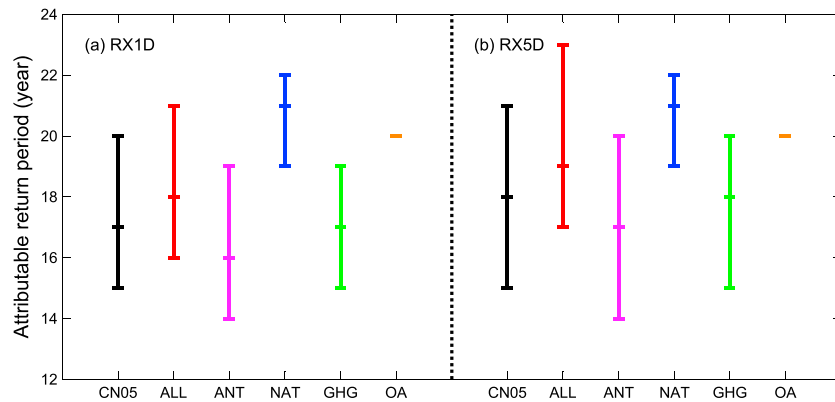


Figure 10. Same as in Figure 9 but for the observed and attributable return periods in 2005 corresponding to the 20 year events in 1961. Units: years.

ANT forcings, 3.05% (−0.50% to 6.86%) for the GHG forcings, 0.13% (0.44% to −0.17%) for the OA forcings, 0.93% (−2.60% to 4.65%) for the ALL forcings, and −0.84% (−2.33% to 0.60%) for the NAT forcings. Therefore, RX1D exhibits a larger percent increase than RX5D, as with the attributable PI changes. Accordingly, the results of the ANT and GHG simulations are coherent with observations concerning the percent changes in extreme precipitation, whereas the results for the ALL simulations are similar but less significant. Although the NAT forcings are associated with smaller attributable values, it cannot be neglected because it can influence ALL through the combined effect of NAT and ANT. Similarly, despite the small attributable values associated with the OA forcings, these forcings can influence ANT through the combined effect of OA and GHG. Thus, the estimated percent increase in extreme precipitation can be attributed to the anthropogenic (ANT, including GHG) forcings to a great extent.

Figure 10 demonstrates the spatially averaged return period in 2005 that corresponds to 20 year events in 1961 based on the selected models. Similar results are obtained when the 15 models are used (see Figure S5). For RX1D (Figure 10a), the observed return period is estimated to be 17 years (15 years to 20 years; 90% confidence intervals), indicating an increased probability of extreme precipitation in recent decades. The return periods for the different forcings are as follows: 16 years (14 years to 19 years) for ANT, 17 years (15 years to 19 years) for GHG, 20 years (20 years to 20 years) for OA, 18 years (16 years to 21 years) for ALL, and 21 years (19 years to 22 years) for NAT. In addition, RX5D exhibits longer return periods than RX1D (see Figure 10b). The observed return period is estimated to be 18 years (15 years to 21 years), approximately a year longer than that of RX1D. Moreover, the estimated values for the different forcings are 17 years (14 years to 20 years) for ANT, 18 years (15 years to 20 years) for GHG, 20 years (20 years to 20 years) for OA, 19 years (17 years to 23 years) for ALL, and 21 years (19 years to 22 years) for NAT. Clearly, extreme precipitation was more likely to occur in 2005, and anthropogenic (ANT, including GHG) forcings provide the best explanation for this phenomenon. Additionally, the ALL simulations also capture the general features of the observations, but the corresponding underestimate of the percent increase in extreme precipitation clearly leads to a longer attributable return period, according to equation (4). However, the results from the NAT simulations bear almost no resemblance to the observations, and there is no change for the OA forcing.

5. Discussion and Conclusions

Previous studies have indicated that extreme precipitation over the midlatitudes of the Northern Hemisphere is expected to increase due to climate warming [Pall et al., 2007; O’Gorman and Schneider, 2009]. Here we briefly discuss the relationship between the changes in annual mean surface air temperature (SAT) and extreme precipitation over China. The SAT over China is reported to have increased significantly in recent decades (1.2°C). This trend is well reproduced by the GHG (1.2°C), ANT (0.9°C), and ALL (1.0°C) simulations, but not by the NAT (0.1°C) simulations or the OA (−0.4°C) simulations (figures not shown). Here we

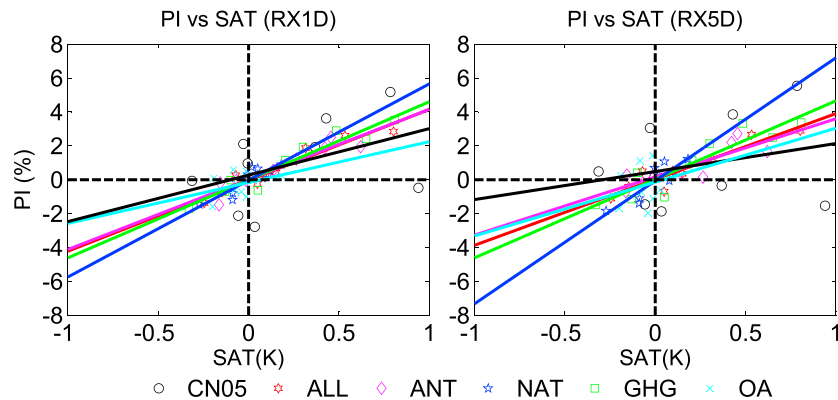


Figure 11. Scatterplots of the 5 year averaged PI anomalies and surface air temperature (SAT) during 1961–2005 from observations and the MME with runs using different forcings for (a) RX1D and (b) RX5D. The solid lines represent the corresponding regression lines obtained by fitting the total least squares equation.

compute the regression coefficient of the 5 year averaged PI and SAT anomalies over China by performing fits using the least squares method. PI is observed to increase by 2.7%/K (−1.2%/K to 6.7%/K) for RX1D and 1.7%/K (−2.7%/K to 6.0%/K) for RX5D, much lower than what the CC relationship predicts. Figure 11 shows scatterplots of the 5 year averaged PI and SAT anomalies averaged over China during 1960–2005 from the observations and the MME. The results of the model simulations indicate that the percent increases in the PI based on RX1D for the different forcings are estimated to be 5.7%/K (3.4%/K to 8.0%/K) for NAT, 4.6%/K (3.7%/K to 5.6%/K) for GHG, 4.1%/K (3.0%/K to 5.3%/K) for ANT, 2.4%/K (−1.8%/K to 6.6%/K) for OA, and 4.2%/K (3.3%/K to 5.1%/K) for ALL. Similar results can be found for RX5D, for which the percent increases for the different forcings are 7.3%/K (4.4%/K to 10.1%/K) for NAT, 4.6%/K (3.2%/K to 6.1%/K) for GHG, 3.4%/K (1.9%/K to 5.0%/K) for ANT, 3.2%/K (−4.1%/K to 10.5%/K) for OA, and 3.9%/K (2.8%/K to 4.9%/K) for ALL. Generally, estimates based on the NAT simulations resemble the CC relationship, but they are considerably higher than the observed percent increases. In contrast, the results of the ALL, GHG, ANT, and OA underestimate the CC relationship but are quite consistent with observations. The relationships between the PI and SAT based on different simulations are quite similar to the above results if we eliminate the last 5 year mean values, which are 5.8%/K (1.7%/K to 9.9%/K) for RX1D and 4.9%/K (0.3%/K to 9.6%/K) for RX5D in the observations, and these changes are much closer to the CC relationship (see Figure S6 and Table S1 in the supporting information). This phenomenon mainly results from the sudden decrease in the PI around the early 2000s, which occurred while SAT continued to increase. Here we multiply the regression ratio by the SAT, and the result is further multiplied by the corresponding scaling factor that describes the response to different forcings. We find that the results based on multiplication are nearly the same as the corresponding values of the attributable PI variability response to the different forcings (Figure 8).

Another issue that should be pointed out is that the ANT fingerprints do not represent a direct response to anthropogenic forcing; instead, they are indirectly estimated as the ALL simulations minus the NAT simulations. By analyzing the single-signal and two-signal cases, we assess the noise present in the ALL and NAT simulations. In addition, the anthropogenic aerosol effect is very difficult to recognize in current models, because both aerosol-cloud interactions and aerosol-radiation interactions can influence extreme precipitation over China [Myhre *et al.*, 2013]. From the perspective of regression model selection, neither the NAT forcings nor the OA forcings are primary elements of predictors; thus, these factors result in invalid single-regression models. However, they are not negligible via the combined external forcing processes. Therefore, physical mechanisms and dynamic processes related to the NAT and OA forcings are worthy of more attention in the future.

In this study, we have found that the ANT results generally capture the observed extreme precipitation changes over China in terms of both their spatial distribution and temporal variations. The results also indicate that the response of the changes in extreme precipitation to the ANT signal is consistent over the past several decades. Meanwhile, the GHG signal is also detectable in cases where RX1D is examined using single-signal analyses. In consideration of the attributable changes in the PI, extreme precipitation, and 20 year

return events under nonstationary climate conditions, we also find that the changes driven by anthropogenic forcing resemble the estimates from observations, as well as the results from the ALL simulations. Consequently, the ANT forcings are likely to partially drive the intensification of extreme precipitation over China, in which greenhouse gas emissions account for the generally detected response. Moreover, the effect of the OA forcings is small, but it cannot be neglected. Despite the good performance of the ANT results, the effects of the ANT forcings could not be detected with doubled internal variability, suggesting that the attribution technique becomes less robust with strong internal variability. Therefore, in addition to the emerging effects of the ANT forcings, the internal variability also has an obvious influence on the intensification of extreme precipitation over China. Furthermore, the ANT results show good agreement with the observations, considering the PI changes in response to climate warming.

Acknowledgments

We sincerely acknowledge the China Meteorological Administration that provided the gridded observations over China that were shared in the website at <http://data.cma.cn/site/index.html>. We also acknowledge the World Climate Research Programme's Working Group on Coupled Modeling, which is responsible for CMIP, and we thank the climate modeling groups (listed in Table 1 of this paper) for producing and making available their model output. For CMIP the U.S. Department of Energy's Program for Climate Model Diagnosis and Intercomparison provides coordinating support and led development of software infrastructure in partnership with the Global Organization for Earth System Science Portals (<https://pcmdi.llnl.gov/>). This research was jointly supported by the External Cooperation Program of BIC, Chinese Academy of Sciences (grant 134111KYSB20150016); the National Key Research and Development Program of China (grant 2016YFA0602401); the National Natural Science Foundation of China (grant 41421004); and the CAS-PKU Joint Research Program.

References

- Aghakouchak, A., L. Y. Cheng, O. Mazdiyasi, and A. Farahmand (2014), Global warming and changes in risk of concurrent climate extremes: Insights from the 2014 California drought, *Geophys. Res. Lett.*, *41*, 151–153, doi:10.1002/2014GL02308.
- Alexander, L. V., et al. (2006), Global observed changes in daily climate extremes of temperature and precipitation, *J. Geophys. Res.*, *111*, D05109, doi:10.1029/2005JD006290.
- Allen, M. R., and S. F. B. Tett (1999), Checking for model consistency in optimal fingerprinting, *Clim. Dyn.*, *15*, 419–434.
- Allen, M. R., and P. A. Stott (2003), Estimating signal amplitudes in optimal fingerprinting, part I: Theory, *Clim. Dyn.*, *21*, 477–491, doi:10.1007/s00382-003-0313-9.
- Bindoff, N. L., et al. (2013), Detection and attribution of climate change: From global to regional, in *Climate Change 2013: The Physical Science Basis. Contribution of Working Group I to the Fifth Assessment Report of the Intergovernmental Panel on Climate Change*, edited by T. F. Stocker et al., pp. 867–952, Cambridge Univ. Press, Cambridge, U. K., and New York.
- Chen, H. P., and J. Q. Sun (2015), Changes in climate extreme events in China associated with warming, *Int. J. Climatol.*, *35*, 2735–2751, doi:10.1002/joc.4168.
- Chen, H. P., and J. Q. Sun (2017), Contribution of human influence to increased daily precipitation extremes over China, *Geophys. Res. Lett.*, *44*, 2436–2444, doi:10.1002/2016GL072439.
- Chen, H. P., J. Q. Sun, X. L. Chen, and W. Zhou (2012a), CGCM projections of heavy rainfall events in China, *Int. J. Climatol.*, *32*, 441–450, doi:10.1002/joc.2278.
- Chen, H. P., J. Q. Sun, and K. Fan (2012b), Decadal features of heavy rainfall events in eastern China, *Acta. Meteorol. Sin.*, *26*, 289–303, doi:10.1007/s13351-012-0303-0.
- Cooley, D., D. Nychka, and P. Naveau (2007), Bayesian spatial modeling of extreme precipitation return levels, *J. Am. Stat. Assoc.*, *102*, 824–840, doi:10.1198/016214506000000780.
- Fan, L. J., and D. L. Chen (2016), Trends in extreme precipitation indices across China detected using quantile regression, *Atmos. Sci. Lett.*, *17*, 400–406, doi:10.1002/asl.671.
- Fischer, E. M., and R. Knutti (2015), Anthropogenic contribution to global occurrence of heavy-precipitation and high-temperature extremes, *Nat. Clim. Change*, *5*(6), 560–564, doi:10.1038/nclimate2617.
- Groisman, P. Y., R. W. Knight, D. R. Easterling, T. R. Karl, G. C. Hegerl, and V. N. Razuvaev (2005), Trends in intense precipitation in the climate record, *J. Clim.*, *18*, 1326–1350, doi:10.1175/JCLI3339.1.
- Handmer, J., et al. (2012), Changes in impacts of climate extremes: Human systems and ecosystems, in *Managing the Risks of Extreme Events and Disasters to Advance Climate Change Adaptation*, pp. 231–290, Cambridge Univ. Press, Cambridge, U. K., and New York.
- Hardwick Jones, R., S. Westra, and A. Sharma (2010), Observed relationships between extreme sub-daily precipitation, surface temperature, and relative humidity, *Geophys. Res. Lett.*, *37*, L22805, doi:10.1029/2010GL045081.
- Katz, R. W. (2013), Statistical methods for nonstationary extremes, in *Extremes in a Changing Climate: Detection, Analysis and Uncertainty*, edited by A. Aghakouchak et al., pp. 15–37, Springer, Netherlands.
- Li, H. X., H. P. Chen, and H. J. Wang (2016a), Influence of North Pacific SST on heavy precipitation events in autumn over North China, *Atmos. Oceanic Sci. Lett.*, *10*, 21–28, doi:10.1080/16742834.2017.1237256.
- Li, H. X., H. P. Chen, and H. J. Wang (2016b), Changes in clustered extreme precipitation events in South China and associated atmospheric circulations, *Int. J. Climatol.*, *36*, 3226–3323, doi:10.1002/joc.4549.
- Liu, R., S. C. Liu, R. J. Cicerone, C. J. Shiu, J. Li, J. L. Wang, and Y. H. Zhang (2015), Trends of extreme precipitation in eastern China and their possible causes, *Adv. Atmos. Sci.*, *32*, 1027–1037, doi:10.1007/s00376-015-5002-1.
- Martins, E. S., and J. R. Stedinger (2000), Generalized maximum-likelihood generalized extreme-value quantile estimators for hydrologic data, *Water Resour. Res.*, *36*, 737–744, doi:10.1029/1999WR900330.
- Min, S. K., X. B. Zhang, F. W. Zwiers, and G. C. Hegerl (2011), Human contribution to more-intense precipitation extremes, *Nature*, *470*, 378–381, doi:10.1038/nature09763.
- Min, S. K., X. B. Zhang, F. W. Zwiers, P. Friederichs, and A. Hense (2009), Signal detectability in extreme precipitation changes assessed from 20th century climate simulations, *Clim. Dyn.*, *32*, 95–111, doi:10.1007/s00382-008-0376-8.
- Mondal, A., and P. P. Mujumdar (2015), On the detection of human influence in extreme precipitation over India, *J. Hydrol.*, *72*, 548–561, doi:10.1016/j.jhydrol.2015.09.030.
- Myhre, G., et al. (2013), Anthropogenic and natural radiative forcing, in *Climate Change 2013: The Physical Science Basis. Contribution of Working Group I to the Fifth Assessment Report of the Intergovernmental Panel on Climate Change*, 683 pp., Cambridge Univ. Press, Cambridge, U. K., and New York.
- O'Gorman, P. A., and T. Schneider (2009), The physical basis for increases in precipitation extremes in simulations of 21st-century climate change, *Proc. Natl. Acad. Sci. U.S.A.*, *106*, 14773–14777, doi:10.1073/pnas.0907610106.
- Pall, P., M. R. Allen, and D. A. Stone (2007), Testing the Clausius–Clapeyron constraint on changes in extreme precipitation under CO₂ warming, *Clim. Dyn.*, *28*, 351–363, doi:10.1007/s00382-006-0180-2.
- Ren, Z. G., M. J. Zhang, S. J. Wang, Q. Fang, X. F. Zhu, and L. Dong (2015), Changes in daily extreme precipitation events in South China from 1961 to 2011, *J. Geogr. Sci.*, *25*, 58–68, doi:10.1007/s11442-015-1153-3.

- Ribes, A., and L. Terray (2013), Application of regularised optimal fingerprinting to attribution. Part II: Application to global near-surface temperature, *Clim. Dyn.*, *41*, 2837–2853, doi:10.1007/s00382-013-1736-6.
- Ribes, A., S. Planton, and L. Terray (2013), Application of regularised optimal fingerprinting to attribution. Part I: Method, properties and idealised analysis, *Clim. Dyn.*, *41*, 2817–2836, doi:10.1007/s00382-013-1735-7.
- Schaller, N., et al. (2016), Human influence on climate in the 2014 southern England winter floods and their impacts, *Nat. Clim. Change*, *6*(6), 627–634, doi:10.1038/nclimate2927.
- Stott, P. A., N. P. Gillett, G. C. Hegerl, D. J. Karoly, D. A. Stone, X. B. Zhang, and F. Zwiers (2010), Detection and attribution of climate change: A regional perspective, *WIREs Clim. Change*, *1*, 192–211, doi:10.1002/wcc.34.
- Stott, P. A., N. Christidis, F. E. Otto, Y. Sun, J. P. Vanderlinden, G. J. Van Oldenborgh, R. Vautard, S. H. Von, P. Walton, and P. Yiou (2016), Attribution of extreme weather and climate-related events, *WIREs Clim. Change*, *7*, 23–41, doi:10.1002/wcc.380.
- Sun, J. Q., H. J. Wang, W. Yuan, and H. P. Chen (2010), Spatial-temporal features of intense snowfall events in China and their possible change, *J. Geophys. Res.*, *115*, D16110, doi:10.1029/2009JD013541.
- Sun, J. Q., and J. Ao (2013), Changes in precipitation and extreme precipitation in a warming environment in China, *Sci. Bull.*, *58*, 1395–1401, doi:10.1007/s11434-012-5542-z.
- Sun, J. S., H. E. Na, G. R. Wang, M. X. Chen, X. N. Liao, and H. Wang (2012), Preliminary analysis on synoptic configuration evolution and mechanism of a torrential rain occurring in Beijing on 21 July 2012 [in Chinese], *Torrential Rain Disasters*, *31*, 218–225.
- Sun, Y., X. B. Zhang, F. W. Zwiers, L. C. Song, H. Wan, T. Hu, H. Yin, and G. Y. Ren (2014), Rapid increase in the risk of extreme summer heat in eastern China, *Nat. Clim. Change*, *4*, 1082–1085, doi:10.1038/nclimate2410.
- Sun, Y., X. B. Zhang, G. Y. Ren, F. W. Zwiers, and T. Hu (2016), Contribution of urbanization to warming in China, *Nat. Clim. Change*, *6*, 706–709, doi:10.1038/nclimate2956.
- Trenberth, K. E., A. G. Dai, R. M. Rasmussen, and D. B. Parsons (2003), The changing character of precipitation, *Bull. Am. Meteorol. Soc.*, *84*, 1205–1217, doi:10.1175/BAMS-84-9-1205.
- Wang, B. L., M. J. Zhang, J. L. Wei, S. J. Wang, X. F. Li, S. S. Li, A. F. Zhao, X. S. Li, and J. P. Fan (2013), Changes in extreme precipitation over northeast China, 1960–2011, *Quat. Int.*, *298*, 177–186.
- Wang, H. J., J. Q. Sun, H. P. Chen, Y. L. Zhu, Y. Zhang, D. B. Jiang, X. M. Lang, K. Fan, E. T. Yu, and S. Yang (2012), Extreme climate in China: Facts, simulation and projection, *Meteorol. Z.*, *21*, 279–304, doi:10.1127/0941-2948/2012/0330.
- Westra, S., L. V. Alexander, and F. W. Zwiers (2013), Global increasing trends in annual maximum daily precipitation, *J. Clim.*, *26*, 3904–3918, doi:10.1175/JCLI-D-12-00502.1.
- Wilks, D. S. (2011), *Statistical Methods in the Atmospheric Sciences*, pp. 105–109, Academic Press, The Boulevard, Langford Lane, Kidlington, Oxford, U. K.
- Wu, J., and X. J. Gao (2013), A gridded daily observation dataset over China region and comparison with the other datasets [in Chinese], *Chin. J. Geophys.*, *56*, 1102–1111, doi:10.6038/cjg20130406.
- Xu, Y., X. J. Gao, S. Yan, C. H. Xu., S. Ying, and F. Giorgi (2009), A daily temperature dataset over China and its application in validating a RCM simulation, *Adv. Atmos. Sci.*, *26*, 763–772, doi:10.1007/s00376-009-9029-z.
- Xu, Y., X. J. Gao, Y. Shi, and B. T. Zhou (2015), Detection and attribution analysis of annual mean temperature changes in China, *Clim. Res.*, *63*, 61–71, doi:10.3354/cr01283.
- Zhai, P. M., X. B. Zhang, H. Wan, and X. H. Pan (2005), Trends in total precipitation and frequency of daily precipitation extremes over China, *J. Clim.*, *18*, 1096–1108, doi:10.1175/JCLI-3318.1.
- Zhang, X. B., and F. W. Zwiers (2013), Statistical indices for the diagnosing and detecting changes in extremes, in *Extremes in a Changing Climate: Detection, Analysis and Uncertainty*, edited by A. AghaKouchak et al., pp. 1–14, Springer, Netherlands, doi:10.1007/978-94-007-4479-01.
- Zhang, X. B., H. Wan, F. W. Zwiers, G. C. Hegerl, and S. K. Min (2013), Attributing intensification of precipitation extremes to human influence, *Geophys. Res. Lett.*, *40*, 5252–5257, doi:10.1002/grl.51010.
- Zwiers, F. W., X. B. Zhang, and Y. Feng (2011), Anthropogenic influence on long return period daily temperature extremes at regional scales, *J. Clim.*, *24*, 881–892, doi:10.1175/2010JCLI3908.1.